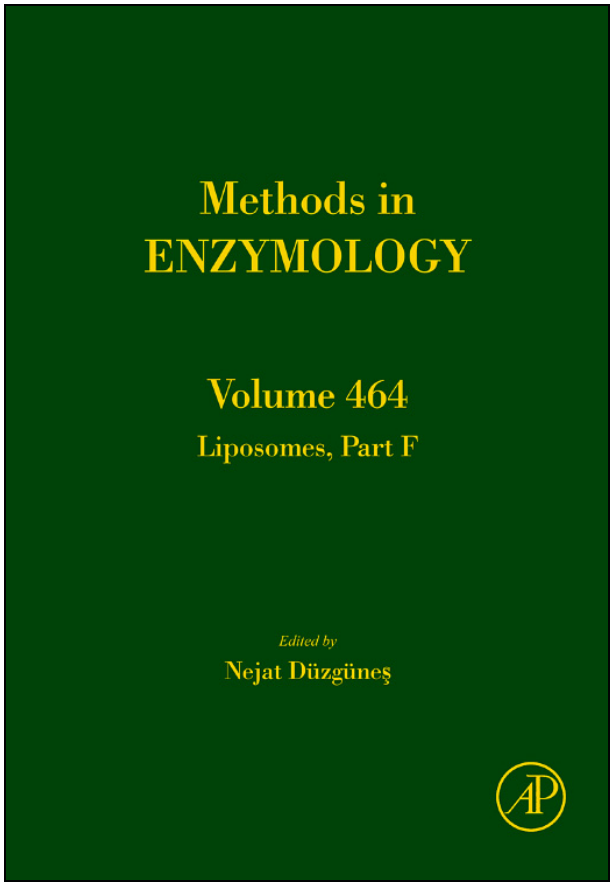

From: Guohui Wu, Alexander Mikhailovsky, Htet A. Khant, and Joseph A. Zasadzinski, Synthesis, Characterization, and Optical Response of Gold Nanoshells Used to Trigger Release from Liposomes. In Nejat Düzgüneş, editor: Methods in Enzymology, Vol. 464, Burlington: Academic Press, 2009, pp. 279-307.
ISBN: 978-0-12-374969-7

CHAPTER FOURTEEN

Synthesis, Characterization, and Optical Response of Gold Nanoshells Used to Trigger Release from Liposomes

Guohui Wu,* Alexander Mikhailovsky,† Htet A. Khant,* *and* Joseph A. Zasadzinski*

Contents

Abstract

Liposomes show great promise as intravenous drug delivery vehicles, but it is often difficult to combine stability in the circulation with rapid, targeted release at the site of interest. Targeting to specific tissues requires developing highly specific ligands with strong affinities to receptors overexpressed on diseased cells; a new cellular target requires developing new ligands and identifying new receptors. Novel photoactivated, hollow, gold nanoshell (HGN)/liposome composites provide a new approach to both controlled

* Department of Chemical Engineering, University of California, Santa Barbara, California, USA
† Department of Chemistry, University of California, Santa Barbara, California, USA

Methods in Enzymology, Volume 464
ISSN 0076-6879, DOI: 10.1016/S0076-6879(09)64014-3

release and specific targeting. HGN are extremely efficient near infrared (NIR) light absorbers, and are not susceptible to photobleaching like conventional dyes. Near-complete liposome contents release can be initiated within *seconds* by irradiating HGNs with an NIR pulsed laser. Targeting the drug is limited only by the dimensions of the laser beam; no specific ligands or antibodies are required, so different tissues and cells can be targeted with the same HGN/liposomes. HGNs can be encapsulated within liposomes or tethered to the outer surface of liposomes for the most efficient drug release. HGNs in liposome solutions can also trigger release, but with lower efficiency. Drug release is induced by adsorbing femto- to nanosecond NIR light pulses that cause the HGNs to rapidly increase in temperature. The resulting large temperature gradients lead to the formation of vapor microbubbles in aqueous solutions, similar to the cavitation bubbles induced by sonication. The collapse of the unstable vapor bubbles causes liposome-membrane rupture and contents release, with minimal damage to the surroundings, and little overall heating of the solution.

1. Introduction

The therapeutic efficacy of many drugs can be improved by maximizing their concentration at the disease site; toxicity can be reduced simultaneously by lowering the concentration elsewhere in the body. Liposomes and other lipid-based drug carriers sequester toxic drugs within a lipid membrane to provide significant advantages over systemic therapy by altering drug biodistribution, maximizing efficacy, while minimizing damage to healthy organs and tissues (Allen and Cullis, 2004; Sengupta *et al.*, 2005). Submicron liposomes and other lipid-based nanocarriers can remain in the bloodstream for extended periods allowing for accumulation in regions of tumor growth or inflammation due to the poorly formed and leaky vasculature, a mechanism known as the enhanced permeation and retention effect (EPR) (Allen and Cullis, 2004). However, it is difficult for a given liposome to combine the necessary physical integrity and drug retention in circulation (to maximize drug accumulation at the disease site) with rapid contents release at the disease site (to affect therapy and minimize drug resistance). For example, liposomal doxorubicin (a chemotherapy drug) reduces drug-related toxicity; however, its therapeutic activity is reduced despite its efficient delivery to tumors because of slow release from the liposome carriers (Abraham *et al.*, 2005). Therefore, one of the current challenges for liposomes and other carriers is how to initiate the release of encapsulated drugs with both spatial and temporal controls. External signals such as ultrasound (Huang and MacDonald, 2004) and visible light (Mueller *et al.*, 2000; Shum *et al.*, 2001) have been used to induce contents release from liposomes, but these methods are limited to surface-accessible areas

such as the eye and skin. For delivery to deeper tissues, other strategies have emerged, ranging from liposomes sensitized to general hyperthermia (Ponce *et al.*, 2006), and receptor-targeted (Noble *et al.*, 2004), and pH- or enzymatically triggered liposomes (Davidsen *et al.*, 2003; Simões *et al.*, 2006). It is difficult, however, to incorporate a destabilizing agent into the liposome membrane to promote release without compromising long-term stability and drug retention in the circulation; by contrast, liposomes optimized to be robust and resistant to leakage in the circulation are hampered by suboptimal drug release. Active targeting requires specific ligands with high affinities to receptors overexpressed on diseased cells that can lead to ''binding-site barriers'' where the tightly bound nanocarriers prevent drug penetration into the tissue (Peer *et al.*, 2007). In addition, targeting a different site requires identifying an appropriate receptor as well as the synthesis and characterization of new ligands.

To address the joint challenges of controlled release and specific targeting, we coupled hollow gold nanoshells (HGNs) that strongly absorb near infrared (NIR) light, to remotely trigger content release from conventional liposomes and ''vesosomes'' (multicompartment lipid-based carriers, or larger liposomes encapsulating multiple smaller liposomes, Kisak *et al.*, 2004) within seconds, using an external, pulsed laser source. The HGNs can be tethered chemically to the liposome surface, encapsulated within the liposomes, or even just be in solution with the liposomes. Absorbing pulsed laser light causes the HGNs to rapidly increase in temperature, leading to the formation of microscopic vapor bubbles (Huang *et al.*, 2006; Tong *et al.*, 2007) in the vicinity of the liposome bilayer, the collapse of these bubbles causes transient liposome membrane rupture and contents release (Wu *et al.*, 2008). The effects on the liposome membrane are similar to those induced by ultrasound-induced cavitation; sonication is a commonly used method to create small, unilamellar vesicles from a lamellar dispersion and is well known to disrupt bilayer membranes. In addition to membrane disruption and fast contents release, only HGN/liposome complexes directly irradiated by the laser are ruptured, providing the necessary spatial control of contents release. Alternatively, continued irradiation of the HGNs can induce localized hyperthermia or permeabilized cell bilayers, both of which can promote drug uptake by cells, or even lead directly to cell death (Chen *et al.*, 2007; Hirsch *et al.*, 2003; Norman *et al.*, 2008; Tong *et al.*, 2007).

The great advantage of NIR to activate liposome drug-release is that tissue, blood, etc. are relatively transparent to 700–1100 nm wavelength light, allowing penetration depths of several centimeters (Weissleder, 2001). Gold nanostructures designed to have a plasmon resonance at NIR wavelengths, that is, silica core/gold nanoshells (Hirsch *et al.*, 2003; Prasad *et al.*, 2005), gold nanorods (Huang *et al.*, 2006; Norman *et al.*, 2008), and HGNs or nanocages (Chen *et al.*, 2007; Prevo *et al.*, 2008; Sun *et al.*, 2003) are especially effective at absorbing NIR light and converting this energy into

heat. HGNs are similar to silica core/gold nanoshells that have been used both *in vitro* and *in vivo* to accumulate NIR light (Hirsch *et al.*, 2003), except that HGNs have a hollow core, which allows easier synthesis, (Prevo *et al.*, 2008) smaller overall dimensions (Prevo *et al.*, 2008; Sun *et al.*, 2003), and no silica to interact with tissues. Gold nanoshells and nanorods illuminated with NIR light have been used successfully to noninvasively heat and eradicate diseased cells and tissues both *in vivo* and *in vitro* (Chen *et al.*, 2007; Hirsch *et al.*, 2003; Huang *et al.*, 2006; Norman *et al.*, 2008; Tong *et al.*, 2007).

Heat-transfer analysis confirms experimental observations that absorption of nano- to femtosecond pulses of NIR light causes the temperature of the HGNs to reach the melting temperature of gold, causing the collapse of the nanoshells into solid nanospheres (Prevo *et al.*, 2008; Wu *et al.*, 2008). The conversion of the optical energy into heat is so fast (nanoseconds) that thermal energy dissipation to the surrounding fluids occurs *after* the HGN reaches its maximum temperature (Link *et al.*, 1999a). As the high-temperature HGNs equilibrate with the surrounding fluid, large-temperature gradients induce the boiling of microscopic amounts of water within microseconds (Lapotko *et al.*, 2006; Lin and Kelly, 1998; Wu *et al.*, 2008). These microbubbles are unstable, and the large volume of cold water surrounding the bubbles causes them to collapse in the same way as sonication-induced cavitation bubbles. The bubble collapse induces mechanical stresses in the surrounding fluid, that can tear lipid membranes apart, thereby releasing the contents of liposomes or other lipid-based drug carriers (Wu *et al.*, 2008). The solution returns to equilibrium less than a millisecond after the initial laser pulse (Wu *et al.*, 2008). Depending on the laser power and the pulse repetition rate, the average solution temperature is increased by no more than a few degrees (Prevo *et al.*, 2008). There is a minimum energy threshold for drug release and a characteristic acoustic response of the solution on irradiation (Wu *et al.*, 2008), similar to sonication-induced cavitation (Lin and Kelly, 1998). Neither the liposomes nor their contents are degraded chemically by the irradiation and release. The potential advantages of this new photoactivated release include (Sengupta *et al.*, 2005) (i) synergistic disease-cell targeting by combining drug-carrying particles (liposomes) and energy-absorbing particles (HGNs) (Allen and Cullis, 2004), (ii) localizing release without harmful effects on surrounding healthy tissues, with no cytotoxicity or cutaneous photosensitivity as in photodynamic therapy, since the gold nanoparticles are inert (Abraham *et al.*, 2005), (iii) triggering up to several centimeters inside the body as most tissues are transparent to NIR light (Huang and MacDonald, 2004), and (iv) creating high-localized concentrations of drug with both spatial and temporal controls. A variety of liposome or polymeric (Discher *et al.*, 1999) carriers could be modified by tethering or encapsulating HGNs to produce a system for rapid, targeted release on demand via NIR irradiation. In

addition, HGN-induced liposome disruption could be used to induce rapid diffusional mixing to permit the study of fast chemical kinetics in nanoenvironments mimicking cell membranes (Chiu *et al.*, 1999).

2. Synthesis of HGNs

The templated galvanic replacement reaction of silver for gold (Chen *et al.*, 2007; Hao *et al.*, 2004; Liang *et al.*, 2005; Prevo *et al.*, 2008; Schwartzberg *et al.*, 2006; Sun and Xia, 2004; Sun *et al.*, 2002; Wiley *et al.*, 2004, 2005) provides a simple and reproducible, nontoxic route to HGNs 20–50 nm in diameter for use in biomedical applications (Scheme 14.1). Silver nanoparticles with diameters of the desired HGN core size are synthesized first, then are sacrificed by adding a gold salt to the solution; the gold is reduced to metal because it has a greater standard reduction potential than the silver template, which is oxidized to a molecular solution (Sun *et al.*, 2002). The gold plates onto the outside of the dissolving silver nanoparticle, resulting in an HGN of controlled diameter; the shell thickness is determined by the relative amount of gold salt to the silver template. The ratio of shell diameter to shell thickness governs the wavelength of the HGN absorbance (Oldenburg *et al.*, 1998); the surface plasmon resonance (SPR) absorbance of nanoshells made in this fashion can be tuned very simply by applying Turkevich's basic colloidal growth chemistry to the sacrificial silver nanoparticles (Link *et al.*, 1999a; Turkevich, 1985; Turkevich *et al.*, 1951, 1954). The emphasis here is not on making shape-specific or extremely monodisperse nanoshells, but rather on a simple and scalable route to nanoshells for practical applications, with tunable sizes and absorbance profiles that require minimal experimental footprints (reduced heating, minimal separations, etc.), and minimal exposure to toxic solvents, reagents, or intermediates that would be detrimental to biomedical applications. The major benefit of this synthesis is that it is

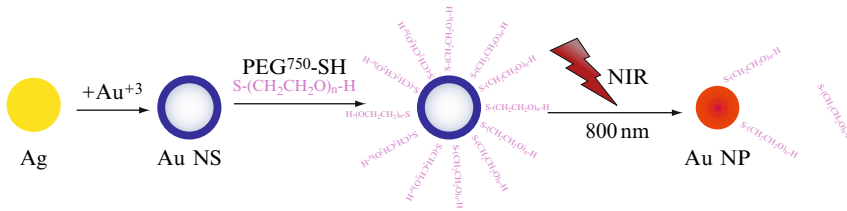

Scheme 14.1 Schematic illustration of the synthesis and stabilization of gold nanoshells as well as their structural change after NIR laser irradiation.

rapid, stable, highly scalable, and in many cases is a true "one-pot" synthesis (Hao *et al.*, 2004; Liang *et al.*, 2005; Sun and Xia, 2004).

Silver templates are prepared at 60 °C in a well-stirred 600 ml solution of 0.2 m*M* silver nitrate ($AgNO_3$; Fisher Scientific, Atlanta, GA) with 0.6 ml 1.0 *M* sodium borohydride ($NaBH_4$; Fisher Scientific) in the presence of 0.5 m*M* sodium citrate (J.T. Baker Chemical Co., Phillipsburg, NJ). The solution is stirred for at least 2 h to allow the $NaBH_4$ to fully hydrolyze. The addition of sodium borohydride accelerates the chemical reactions, and the resulting nanoparticles are ~15–25 nm in diameter (Prevo *et al.*, 2008). After cooling to room temperature, larger silver nanoparticles could be grown from these stock sols, if desired. Silver particle growth is initiated by adding 0.5 ml of 2.0 *M* hydroxylamine hydrochloride solution ($NH_2OH{\cdot}HCl$, Aldrich, Milwaukee, WI) to the silver sol, followed by stirring for 5 min (Turkevich, 1985; Turkevich *et al.*, 1951, 1954), addition of 1.25 ml 0.1 *M* $AgNO_3$ (0–1 ml), and stirring overnight. The growing silver nanoparticles turn the sol a darker yellow or orange, depending on the amount of additional $AgNO_3$. Gold nanoshells could then be made via galvanic replacement chemistry from the template silver sols without the need to isolate the silver nanoparticles.

First, a given silver sol (50 ml) is heated to 60 °C and the necessary amount (3.2 ml for the nanoshells in Fig. 14.1) of 25 m*M* tetrachloroauric acid ($HAuCl_4$, Aldrich) is added dropwise (depending on the initial silver template size). Silver (Ag^+/Ag 0.8V, vs. SHE) has a lower redox potential than gold ($AuCl_4^-/Au$ 0.99V, vs. SHE) and the replacement reaction is (Sun *et al.*, 2002):

$$3Ag_{(s)} + AuCl_{4(aq)}^{-} \rightarrow Au_{(s)} + 3Ag_{(aq)}^{+} + 4Cl_{(aq)}^{-}$$

Upon the addition of the concentrated $HAuCl_4$, the solution turns from yellow/orange to gray/yellow to blue/gray to blue/turquoise within seconds as the silver and gold are oxidized and reduced, respectively. The reactions are monitored using UV/vis/NIR spectroscopy, and stopped when the silver peak located near 400 nm vanishes (usually within a few minutes, although the reaction mixture is generally stirred for at least 1 h after gold addition). This which occurs when the gold/silver ratio in the reaction vessel approaches the stoichiometric ratio of 1:3 (to err on the side of completion, the ratio is usually 37:1). Once the reaction is complete, the samples are cooled, silver chloride is allowed to precipitate, and the supernatant containing the gold nanoshells are transferred to another vessel and stored at 4 °C until further use. The size distribution and particle morphology are analyzed by transmission electron microscopy using an FEI Tecnai T20 microscope (Fig. 14.1). A typical HGN is spherical and hollow, although some have irregular shapes or incomplete shells. This particular set of concentrations gave HGNs of diameter 33 ± 13 nm and shell

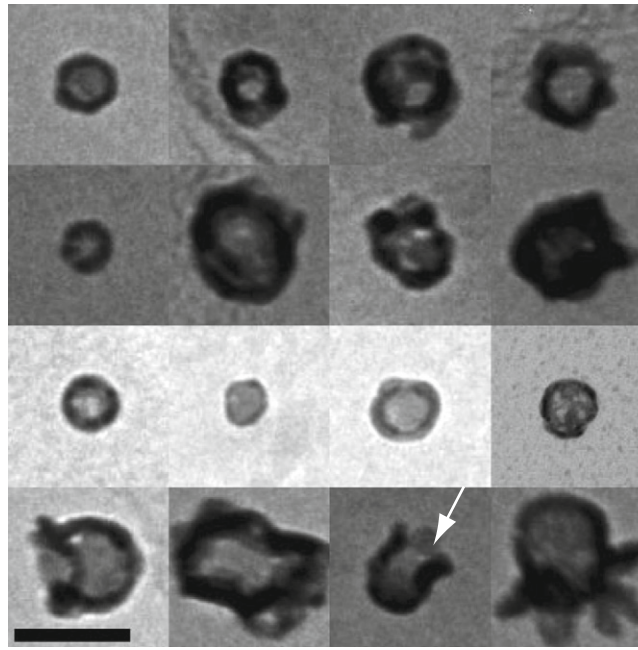

Figure 14.1 TEM images of HGNs with a variety of morphologies. All of the nanoshells have a hollow core, that is, the light gray area near the center of each nanoshell, surrounded by the gold shell, which is dark gray to black. Some nanoshells are not complete (arrow). Bar is 50 nm.

thicknesses of 2 ± 0.9 nm, and had a maximum adsorption around 820 nm (see Fig. 14.7) using a Jasco V-530 UV/vis spectrometer (JASCO Corp., Tokyo).

The synthesized HGNs are quite stable in the dilute synthesis solutions because of electrostatic repulsion caused by the adsorption of citrate ions, resulting in an overall negative charge on the HGN. However, to improve their stability against aggregation in physiological buffers and other high-ionic strength solutions, the HGNs are further stabilized sterically by tethering poly(ethylene glycol) (PEG) of molecular weight 750 Da to the HGN via a thiol linker. Methoxypolyethylene glycol amine (^{750}PEG-NH_2, PEG molecular weight of 750 Da, Aldrich) is converted to methoxypolyethylene glycol thiol (^{750}PEG-SH), using a twofold molar excess of 2-iminothiolane·HCI (also known as Traut's reagent; Sigma-Aldrich, St. Louis, MO) in buffer (2.28 m*M* Na_2HPO_4, pH 8.8). One-half milliliter of the prepared 0.0379 *M* ^{750}PEG-SH is added to 600 ml of the HGN to achieve a 1000:1 ratio of thiol:gold. The PEG-stabilized HGN solution is centrifuged at 21,000×*g* for 30 min and redispersed in Milli-Q water twice to remove any unattached and/or soluble chemicals. The pellet readily redisperses in

buffer. Complete gold nanoshells and nanorods with various coatings can also be purchased directly from Nanopartz Co. (Salt Lake City, Utah).

In our case, the PEG-modified HGNs are stable for at least 1 year in physiologic buffers (longer term stability is still being tested). No flocculation is observed after mixing the HGN solution with concentrated carboxyfluorescein (CF) in buffer at basic pH; severe precipitation occurs instantly for HGNs without ^{750}PEG-SH. For *in vivo* applications, PEG coatings can minimize recognition by the immune system and minimize nonspecific binding to blood proteins and cells. Similar PEG-modified gold nanoparticles show little cytotoxicity *in vitro* (Niidome *et al.*, 2006). After intravenous injection, PEG-modified gold nanoparticles circulate in mice with a half-life of approximately 1 h, and, for at least 72 h, there is no accumulation in major organs except for the liver (Niidome *et al.*, 2006). The free methoxy end of the ^{750}PEG-SH can also be modified to display various ligands or antibodies to allow the HGNs to be tethered to various lipids or proteins.

Unlike gold nanorod syntheses, this approach does not require the shape-determining detergent hexadecyltrimethylammonium bromide (CTAB), which is cytotoxic. CTAB adsorbs to gold very strongly and it is difficult to replace CTAB with other ligands; removal of CTAB can result in nanoparticle aggregation (Niidome *et al.*, 2006). An additional advantage of this galvanic replacement synthesis is the small size of the HGNs, which is especially useful when enclosing HGNs within liposomes for controlled release. In comparison, the silica core/gold shell nanoparticles pioneered by Hirsch *et al.* (2003) are at least 100 nm in diameter, and the dielectric core material (either silica or polystyrene) brings the additional concern of potential biological effects of silica or the products of silica degradation. An added benefit is that, compared with the one-pot synthesis of HGNs, the silica core/gold shell nanoparticle synthesis is time-consuming and labor-intensive (Shi *et al.*, 2005).

3. Optimization of HGN Dimensions for Maximum Absorption in the NIR

An idealized HGN structure allows for analytical predictions of light absorption and scattering by means of classical field theories, such as the Mie scattering formalism (Kreibig and Genzel, 1985). Analytical solutions exist for the interaction of light with spherical metal nanoparticles, nanoshells, and nanorods, that is, structures possessing a high degree of symmetry. The optical properties of less symmetric particles or aggregates require numerical solutions of Maxwell's equations. For spherical shell nanoparticles such as HGNs, analytical solutions for the far-field extinction, absorption, and scattering cross sections have been known for almost a century and can be found, for

example, in the classic book by Bohren and Huffman (1983). These cross sections are related to the attenuation of photons, N, according to $N/N_0 = \exp(-n\sigma_{ext}x)$, in which σ_{ext} is the HGN extinction cross section, n is the number/volume of HGN, and x is the path length of light with initial number of photons, N_0. The extinction cross section is the sum of the scattering cross section, σ_{sca}, and absorption cross section, σ_{abs}, of the incident light.

To model the absorption and scattering of HGNs, analytical solutions of Mie scattering for core/shell nanoparticles can be used as described by Bohren and Huffman (1983). The dielectric function (or complex index of refraction) for gold is taken from various sources (Johnson and Christy, 1972), but similar results are obtained for all sets of material properties. The *extinction efficiency*, Q_{ext}, is the ratio of the extinction cross section to the geometric cross section: $Q_{ext} = \sigma_{ext}/\pi a^2$, a is the HGN radius. The absorption efficiency, Q_{abs}, is the difference between Q_{ext} and Q_{sca}, the scattering efficiency: $Q_{abs} = Q_{ext} - Q_{sca} = \sigma_{abs}/\pi a^2$. Ideally, all of the radiation would be adsorbed by the HGN ($Q_{abs} >> Q_{sca}$) to provide the maximum HGN heating. The light scattered by the HGNs is lost for useful purposes. Figure 14.2 shows the absorption and scattering efficiencies as a function of wavelength for an idealized HGN with an overall diameter of 33 nm and a shell thickness of 1.7 nm. For wavelengths around 800 nm, absorption dominates scattering for these HGNs, suggesting that almost all of the laser energy is being converted to heat. The peak value of the absorption cross section for an HGN with these dimensions is 9.12×10^{-11} cm^2.

Figure 14.3 shows the calculated optimal shell thickness d as a function of the HGN diameter D. HGNs with these dimensions exhibit the maximum

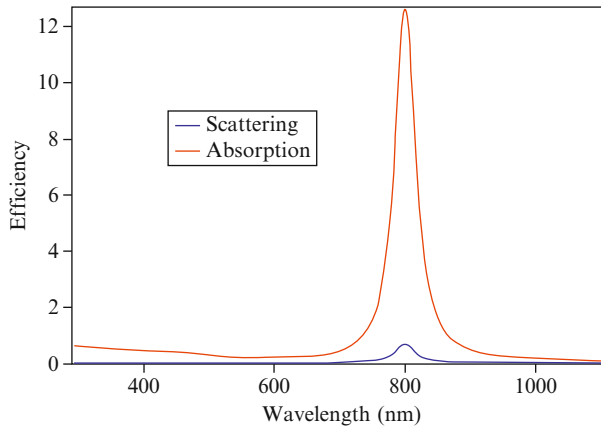

Figure 14.2 Theoretical absorption and scattering efficiency for HGN with a diameter of 33 nm and shell thickness of 1.75 nm in water.

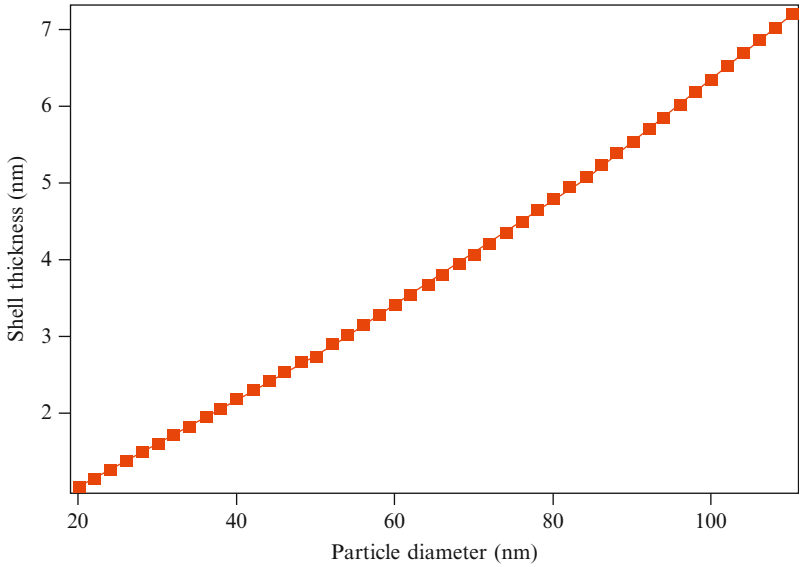

Figure 14.3 Optimal shell thickness providing the maximum absorption efficiency at 800 nm as a function of HGN diameter.

absorption at 800 nm (optimal wavelength for a Ti:Sapphire laser). This result shows that the smaller the HGN, the thinner the gold shell must be to insure a maximum adsorption in the NIR range of the optical spectrum. For example, a 40-nm diameter HGN should have a shell thickness of ~2 nm, while an 80-nm diameter HGN should have a shell thickness of ~5 nm to maximize the absorption at 800 nm.

Figure 14.4 shows the calculated size-dependent absorption efficiency, Q_{abs}, and absorption cross section, σ_{abs} at 800 nm. The absorption efficiency peaks for HGNs with $D \sim 50$ nm, but the absorption cross section peaks for $D \sim 85$ nm. For a given mass of gold, the HGN with the highest efficiency should be chosen as the mass/HGN increases faster with HNG diameter than does the optical cross section. The peak absorption cross section is $\sim 4 \times 10^{-10}$ cm^2. For an optical energy density of 2.2 mJ/cm^2 corresponding to the cavitation threshold, HGN of any size will be heated well above the melting point of bulk gold (Prevo *et al.*, 2008). Smaller HGN will be heated to higher temperatures due to their smaller mass, but particles with $D \sim 85$ nm will absorb the maximum energy/particle (Prevo *et al.*, 2008). Thus, it is difficult to predict *a priori* which HGN size is optimal for a given application.

While the direct implementation of Mie theory does a good job of predicting the wavelength at which the maximum absorbance occurs for the experimentally determined HGN size distribution (Fig. 14.5), it fails to

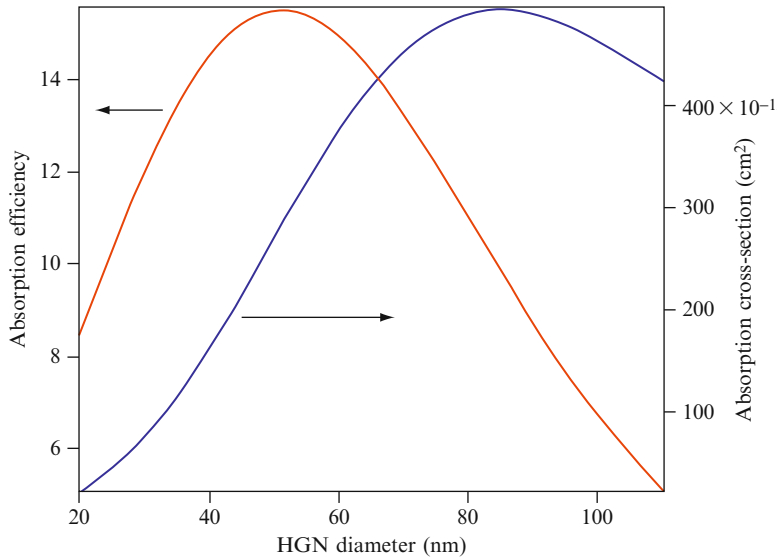

Figure 14.4 Absorption efficiency (red) and cross section (blue) at 800 nm of HGNs with optimized geometry as a function of diameter.

describe the inhomogenously broadened extinction spectrum of the HGN ensemble (Fig. 14.6). The statistical distribution of shell thickness and HGN diameter are determined from the TEM micrographs and fit by a log-normal distribution function (Fig. 14.5). The extinction cross section of the HGN ensemble has been modeled using these distribution functions. Figure 14.6 shows that the simulation predicts less broadening of the absorption spectra than what is observed experimentally. The experimental broadening may be due to the shape polydispersity, as well as possible chemical variations due to any residual silver alloy in the HGN. An additional complication is that the shell thickness in the HGNs is significantly less than the electron mean free path in gold (~50 nm), and the dielectric function can be strongly affected by the scattering of electrons at the nanoparticle boundaries. To address this effect a size-dependent term is introduced into the dielectric function of gold according to Alvarez *et al.* (1997) and the simulation optimized numerically to achieve the best match between the experimental extinction spectra and the theoretical model. The use of the size-dependent dielectric function does not resolve completely the discrepancy between the experimental and theoretical extinction spectra. This may be explained by the fact that thin layers on the metal surface may be depleted/enriched in electron density (also the silver alloying), depending on the properties of the environment, which can change the effective dimension of the HGN (Kreibig, 1995).

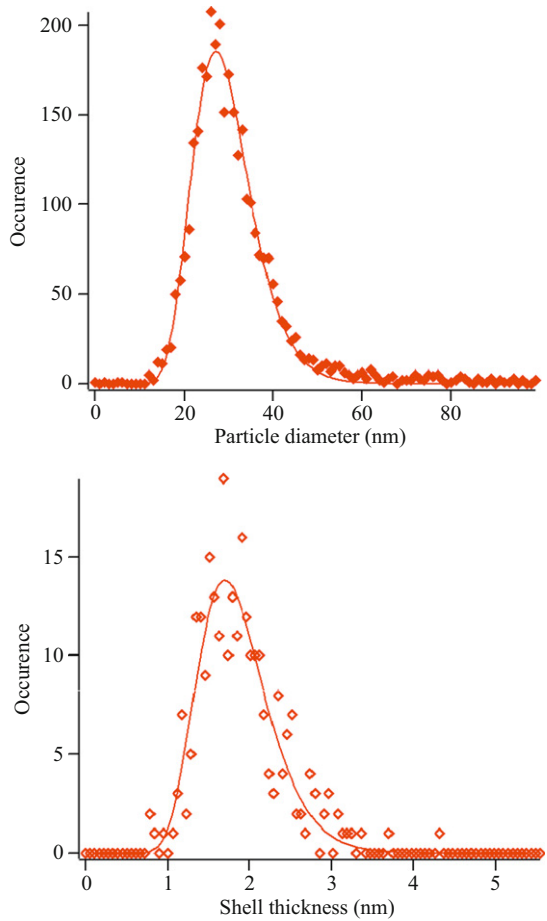

Figure 14.5 Measured diameter (left) and shell thickness (right) from TEM images for HGNs synthesized as described in text.

4. HGN Response to Femtosecond NIR Laser Pulses

The HGNs prepared as discussed above have a broad absorption peak at 780–820 nm (Figs. 14.6 and 14.7), which overlaps well with the Ti: Sapphire pulsed laser (Spectraphysics Spitfire), which has an FWHM of ~12 nm centered around 800 nm. Compared with conventional dyes, HGNs are much stronger than NIR absorbers and are less susceptible to photobleaching or other forms of chemical degradation. However, sufficient irradiation does lead to collapse of the HGN into solid gold

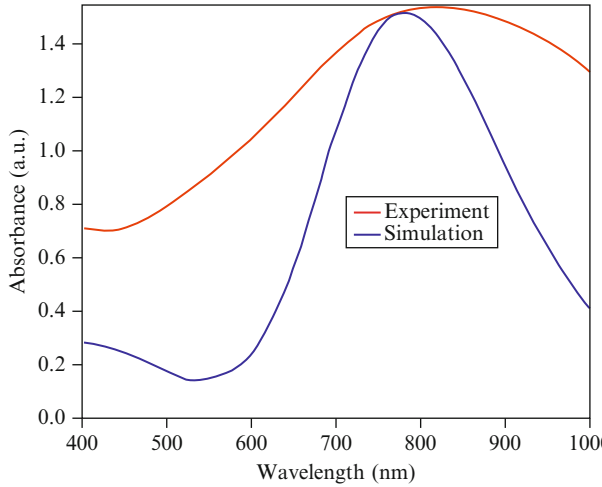

Figure 14.6 Measured (red) and calculated (blue) extinction spectra of the experimental distribution of HGN diameters and shell thicknesses from Fig. 14.5.

nanoparticles; this collapse leads to a loss of absorption in the NIR (Fig. 14.3). The original color of the HGN suspensions is dark blue (Fig. 14.7); after pulsed NIR laser irradiation at 800 nm at a power density of 16.1 mJ/cm^2 for 8 min (120fs pulses at 1 kHz repetition rate), the HGN suspension turns a dark red color. The corresponding UV–VIS absorption spectra exhibit a shift of the absorption peak from 780 to 470 nm, indicating the conversion of the HGN to solid nanoparticles (Prasad *et al.*, 2005; Prevo *et al.*, 2008). TEM images of irradiated particles confirm the change in the HGN morphology; the hollow center of the nanoshell collapses and the particles anneal into the more stable solid spheres, consistent with the change in color and the shift of the adsorption maxima (Fig. 14.7).

These observations confirm that HGNs reach sufficiently high temperatures after femtosecond pulses of NIR light to melt and anneal into more stable shapes. For a solid-core, spherical Au particle with size from 2 to ~100 nm, the SPR is from 520 to 570 nm (Kreibig, 1977). For other gold morphologies, such as rods, cages, thin plates, and aggregates, the absorption peak due to the SPR shifts to lower energy (higher wavelength) in the NIR window. The peak at 470 nm can be explained by the formation of Au–Ag alloy nanoparticles during the laser-induced heating. Ag has an SPR at 400 nm; the plasmon absorption of Au–Ag alloy falls between the SPRs of Ag and Au nanoparticles and varies linearly with the Au mole fraction (Link *et al.*, 1999b). X-ray photoelectron spectroscopy confirms the presence of residual silver in the HGN (Prevo *et al.*, 2008). A second explanation for the 470-nm peak is the presence of Au clusters less than 2 nm in size

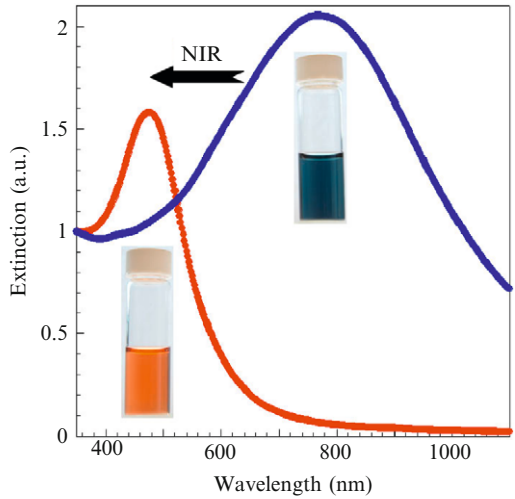

Figure 14.7 Extinction spectra (normalized at 350 nm) of: (blue) HGN suspension; (red) HGN suspension laser-irradiated at a power density of 16.1 mJ/cm^2 for 8 min (120 fs pulses at 1-kHz repetition rate). Below the peaks of extinction curves are photographs of the corresponding dispersions. The spectra are consistent with the collapse and annealing of the HGN into solid gold/silver alloy nanoparticles.

due to laser-induced particle heating and fragmentation (Link *et al.*, 1999b). The existence of such fine Au particles has also been postulated to explain the similar absorption peak at 460 nm of Au/SiO_2 after ultrasound treatments (Link *et al.*, 1999b).

Rapid nonradiative relaxation processes convert the absorbed light energy mainly to heat (Grua *et al.*, 2003). Petrova *et al.* (2006) found that at temperatures higher than 250 °C, nanorods anneal into spherical particles in less than 1 h; we have found that HGN also anneals into solid particles within hours at 250 °C. This is significantly below the melting point of bulk gold (1064 °C). Time-resolved spectroscopy studies, however, showed that nanorods (in aqueous solution) maintained their shape in spite of a rapid lattice temperature increase to 1000 K achieved by ultrafast pulsed laser excitation. Petrova *et al.* (2006) explained that "the difference in the temperature stability of the nanorods under continuous thermal heating compared to laser-induced heating is attributed to thermal diffusion: the rods do not stay hot for long enough after ultrafast excitation for significant structural transformation to occur." On the other hand, the melting of HGN suggests that the structural changes in HGN after femtosecond laser-induced heating requires that the temperature in the HGN gold lattice must be significantly higher than 1000 K. The amount of rearrangement required to collapse an HGN into a solid sphere is also much less than that required to change a solid gold nanorod to a sphere.

The maximum temperature reached by the HGNs is also limited by the rate of energy dissipation into the surrounding liquid. However, the thermal diffusivity of water limits the conduction of heat from the HGNs, and heat dissipation from the HGN to the surrounding water is much slower (microseconds) than the electron dynamics involved in plasmon-mediated heating (nanoseconds) (Link *et al.*, 1999a; Prasad *et al.*, 2005; Prevo *et al.*, 2008; Roper *et al.*, 2007). Essentially, all of the optical energy input to the HGN goes into heating the HGN (Prevo *et al.*, 2008). The high temperature HGN then dissipates its thermal energy into the surrounding water by conduction; large temperature gradients are generated in the vicinity of the HGN, which cause the surrounding water to boil and form rapidly growing microbubbles. These microbubbles cannot grow indefinitely as there is not sufficient energy within the HGN to raise the bulk of the solvent to the boiling temperature (Prevo *et al.*, 2008). The bubbles become unstable and can undergo a violent collapse which produces shock waves (Pecha and Gompf, 2000) or microjets (Popinet and Zaleski, 2002). Recent time-resolved X-ray scattering experiments show that femtosecond laser excitation of gold nanoparticles leads to the compression of the solvent, which is consistent with bubble formation (Kotaidis *et al.*, 2006).

The growth and collapse of unstable vapor bubbles also produces a detectable pressure change in the bulk solution, which gives a photoacoustic signal that can be ''heard'' by a hydrophone (Model #TC4013, Reson, Goleta, CA). The bandwidth of the hydrophone is 1 Hz–170kHz. The hydrophone, which is 0.5 cm in diameter and $\sim$2 cm long, is immersed into the HGN solution $\sim$5 mm above the laser beam in a quartz cuvette with 10-mm light path. The solution volume is 2.5 ml. The sample is not stirred during the laser irradiation to minimize the acoustic noise. Data collection is synchronized with the laser cavity dumping event by using triggering signal from the laser control electronics, and the output of the hydrophone is collected by a digital oscilloscope (Tektronix TDS5032B). The acoustic transients are averaged over several hundred individual laser pulses to improve the signal/noise ratio.

Figure 14.9A shows a typical acoustic signal of pressure fluctuations in a 0.142 m*M* HGN solution as recorded by a hydrophone between two 130 fs laser pulses (1-KHz repetition rate). No pressure fluctuations above background occurred in control solutions of phosphate buffer solution, or 4.71 μM CF solution dissolved in phosphate buffer, irradiated with the highest pulsed laser power density of 16.2 W/cm^2 (Fig. 14.9B).

Laser-induced heating, however, does not always produce an acoustic signal. For spherical gold particles in aqueous solution, explosive boiling happens only above a threshold temperature of $\sim$85% of the critical temperature (T_c = 374 °C for water) (Kotaidis *et al.*, 2006). We have observed that a similar threshold of the laser energy density is required to generate a photoacoustic signal. The amplitude of the pressure fluctuations remains at

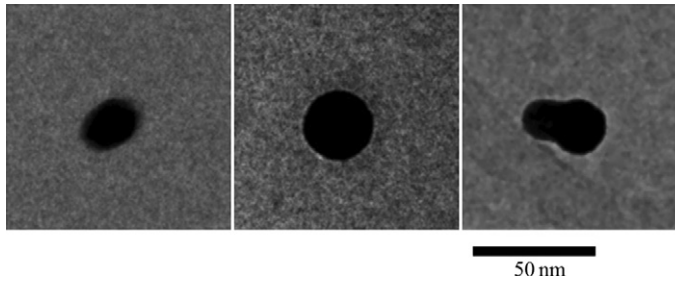

Figure 14.8 TEM images showing the collapse of the HGN into solid nanoparticles after 16.1 mJ/cm^2 NIR-laser irradiation.

background up to a laser power density of ~2.3 mJ/cm^2, above which the amplitude of the pressure fluctuations increases with increasing laser power density (Lin and Kelly, 1998) (Fig. 14.9A). Calculations show that the increased power density leads to higher HGN temperatures (Prasad *et al.*, 2005; Prevo *et al.*, 2008), which are then translated into larger pressure fluctuations (more water boils and larger bubbles are formed) as this energy is dissipated. The pressure fluctuations die out within a few hundred microseconds after the light pulse; the HGN and the surrounding solution equilibrate and return to ambient temperature prior to the next pulse from the laser.

Although the gold nanoshells melt (Fig. 14.8), the temperature increase of the bulk solution is small; the sample reaches a steady temperature only a few degrees above ambient, which depends on the laser power density and the HGN concentration. This is because the absolute amount of energy deposited into the solution is quite small (the laser power here is 0.67 W). Therefore, any significant pulsed laser-induced heating is limited to the immediate vicinity (microns) of the HGNs. This is important for the biomedical application of HGNs as only liposomes, vesosomes (liposomes encapsulating multiple smaller liposomes), or tissues directly adjacent to the irradiated HGNs will be affected by the light pulse. However, it is well established that transient cavitation bubbles due to sonication are capable of disrupting cell and liposome membranes (Huang, 2008). The irradiated HGNs might be thought of as optically triggered, nanosonicators, which can cause the transient rupture of liposomes resulting in rapid contents release.

5. Coupling HGN to Liposomes

As the extent of the heated zone is quite small, the method of coupling the HGN to liposomes or cell membranes is important. We have examined three different methods of rupturing liposomes with HGNs. First, HGNs

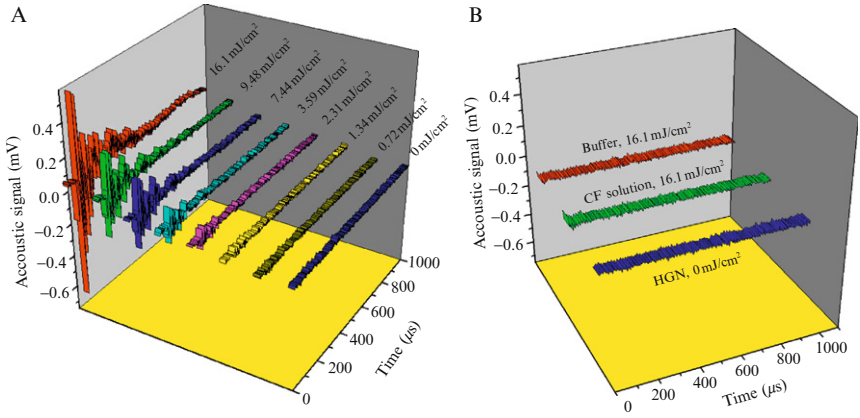

Figure 14.9 Acoustic signal amplitude of (A) 0.142 m*M* HGN solution as a function of pulsed laser energy is recorded by a hydrophone after a single laser pulse of various laser energy densities. The magnitude of the photoacoustic signal of pressure fluctuations associated with cavitation (Paliwal and Mitragotri, 2006) increases with increasing laser power density, consistent with larger energy absorption by the HGN and subsequent larger or more numerous cavitation bubbles. However, a threshold value of laser-energy density of 2.3 mJ/cm^2 is required to induce the photoacoustic signals above background in the HGN solutions. (B) Acoustic signal amplitude in control solutions. No signal was observed in buffer or CF solution without HGN, and no signal was observed in HGN solution without laser irradiation.

can be encapsulated within dipalmitoylphosphatidylcholine (DPPC) liposomes via the interdigitated phase transition, which causes lipid membranes to form flat open sheets at low temperatures that close to form unilamellar vesicles at higher temperatures (Boyer and Zasadzinski, 2007; Kisak *et al.*, 2002) (Scheme 14.2A). Second, the nanoshells can be tethered to the outside of preformed liposomes using a thiol/PEG–lipid linkage (Scheme 14.2B). Third, the HGN solutions can be mixed with preformed liposomes so that the HGNs are exclusively outside the liposomes (Scheme 14.2C).

Scheme 14.2A: Encapsulation of HGN and CF inside liposomes. 6-Carboxyfluorescein (50 m*M*) (CF; Invitrogen; Eugene, OR) is dissolved in water together with 6 equiv. of concentrated NaOH, which converts the CF from its acid form to the water-soluble salt form. The CF solution is used to disperse the PEG-stabilized HGNs described previously. Liposomes are prepared as described by Boyer and Zasadzinski (2007) and Kisak *et al.* (2002). DPPC dried from chloroform is hydrated with Milli-Q water by vortexing at 55 °C to form a lamellar dispersion, which is then cooled to room temperature. Vesicles are prepared by sonication at room temperature using a 60 Sonic Dismembrator (Fisher Scientific) for 4 min at a power of 4 W.

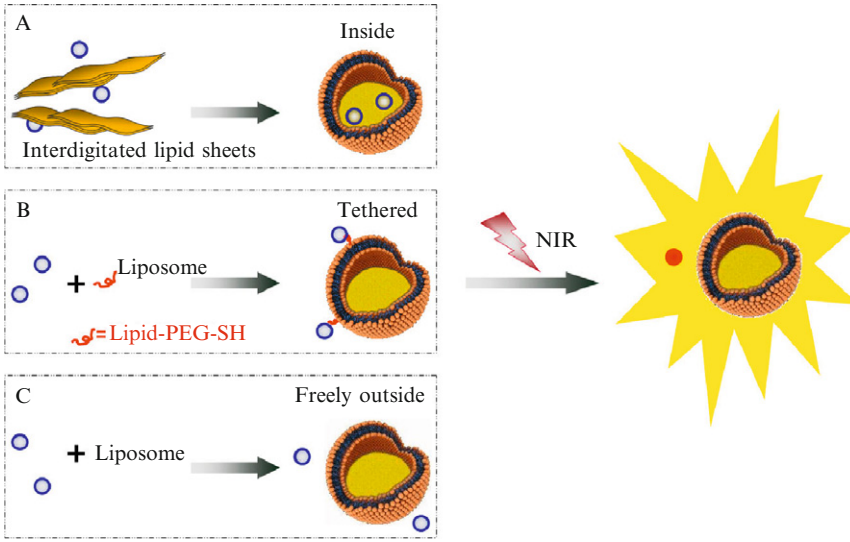

Scheme 14.2 HGNs can be located: (A) inside the liposomes; (B) tethered to the liposomes; and (C) free outside the liposomes.

At room temperature, DPPC bilayers are in the gel or $L_{\beta'}$ phase; the interdigitated bilayer phase (L_I) is induced by the addition of 0.106 ml of ethanol (3 *M* net ethanol concentration) to 0.5 ml of a 50 mg/ml DPPC vesicle suspension. The initially bluish vesicle suspension turns milky white, and its viscosity increases significantly. The vesicles fuse and burst open, forming stacks of open bilayer sheets many micrometers in size (Boyer and Zasadzinski, 2007; Kisak *et al.*, 2002). After annealing at 4 °C overnight, the interdigitated sheets are centrifuged at 3000×*g* and dispersed in pure water three times to remove any ethanol. The pellet of interdigitated DPPC sheets is mixed with the solution of 32 m*M* CF and 12 m*M* HGN and heated at 50 °C for 2 h under vortex mixing. Raising the temperature causes a phase transition from L_I to the liquid crystalline L_α phase and the bilayer sheets become much more flexible, allowing them to close around the HGN in suspension to form interdigitation–fusion vesicles (Boyer and Zasadzinski, 2007; Kisak *et al.*, 2002). The internal concentrations in the liposomes are 32 m*M* CF (110 mOsm), 12 m*M* HGN, and the overall lipid concentration is 22 mg/ml DPPC. Based on earlier work (Boyer and Zasadzinski, 2007), about 50–60% of the HGN is encapsulated in liposomes. Cryo-EM confirms that the HGN are encapsulated within the liposomes by this procedure (Wu *et al.*, 2008).

After encapsulation, phosphate-buffered saline (PBS; 20 m*M* Na_2HPO_4/NaH_2PO_4, 34.5 m*M* NaCl, pH = 7.4) is used to disperse the liposomes to minimize osmotic stress across the membrane. The unencapsulated CF is

removed by size-exclusion chromatography using a Sephadex G-75 column (Amersham Biosciences Corp., Piscataway, NJ) eluted with PBS buffer. The eluted suspension is centrifuged at $100\times g$ for 20 min and redispersed in PBS buffer twice to remove any unencapsulated HGN prior to irradiation.

Scheme 14.2B: Tethering HGN to liposomes containing CF. A pellet of interdigitated DPPC sheets is prepared as described above. The interdigitated sheets are mixed with a 32 m*M* CF in water solution containing 2 mol% (relative to the amount of DPPC used) DSPE-^{2000}PEG-NH_2 powder (Avanti Polar Lipids, Alabaster, AL). The mixture is then heated at 50 °C for 1 h under vortex mixing. The DSPE-^{2000}PEG-NH_2 partitions into the DPPC bilayers in the L_α phase as the temperature increases and the interdigitation fusion vesicles are formed (Sou *et al.*, 2000; Zalipsky *et al.*, 1996). Next, the amine groups at the liposome surfaces are converted to thiol by mixing with 100% excess 2-iminothiolane solution (0.29 *M*). The thiolated liposomes encapsulating CF are incubated with a solution of HGN and CF for 48 h to allow HGN to tether via the thiol linkages to the outer surfaces of liposomes. The final concentrations in the solution are 18 mg/ml phospholipid (98 mol% DPPC and 2 mol% DSPE-^{2000}PEG-SH), 18 m*M* HGN and 32 m*M* CF. The liposomes with tethered HGNs are eluted through a Sephadex G-75 size-exclusion column to remove any unencapsulated CF, and centrifuged at $200\times g$ to remove untethered HGNs.

Figure 14.10 shows a cryo-EM tilt series that confirms that the HGN are tethered to the liposomes (Wu *et al.*, 2008). Thin films of the liposome/HGN solution are spread on holey carbon TEM grids (Structure Probe, West Chester, PA) under controlled temperature and humidity conditions using a VitRobot (FEI Company, Hillsboro, OR) (Frederik and Hubert, 2005), then vitrified by rapid plunging into liquid ethane (Chiruvolu *et al.*, 1994a,b; Frederik and Hubert, 2005; Jung *et al.*, 2002). Cryo-EM imaging is performed on an FEI Tecnai T20 microscope, operating at 200 kV with a Gatan liquid nitrogen specimen cryo-holder. Single-axis tomographic imaging is performed with a JEOL 2010A microscope from $-60°$ to $+60°$ tilt

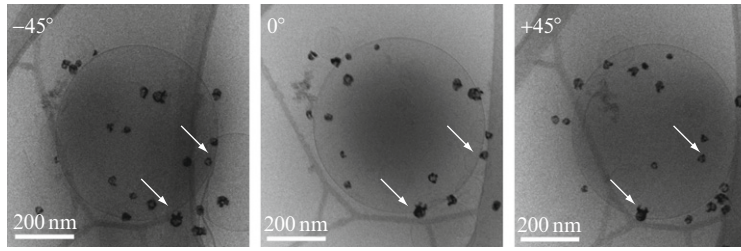

Figure 14.10 Cryo-TEM tilt series showing that the HGNs are tethered to the liposome surfaces. Arrows point out the same HGNs as they rotate with the surface of the liposome.

angles in 2° increments with a total dose of less than 100 electrons/Å^2. Three representative images at goniometer tilt angles of −45°, 0°, and 45° are shown in Fig. 14.10. The arrows mark specific HGNs on the surface of the liposomes followed during the 90° rotation to confirm that HGNs are tethered to the surface.

Scheme 14.2C: Liposomes containing CF with external HGNs. DPPC liposomes containing 32 m*M* CF are prepared by the same interdigitation–fusion method described earlier, except no HGNs are added to the solution prior to vesicle formation. The preformed vesicles are eluted through a Sephadex G-75 column to remove external CF, and then dispersed in different concentrations of HGN solutions as needed.

5.1. Pulsed laser optics

Liposome disruption is triggered by irradiating the liposome/HGNs with the output of the femtosecond Ti:Sapphire regenerative amplifier (Spectraphysics Spitfire) running at a repetition rate of 1 kHz. The setup is illustrated in Fig. 14.11. The laser beam is collimated by a Galilean telescope to achieve a Gaussian diameter of 2.3 mm. The pulse duration is monitored by a home-built single-shot optical autocorrelator and is kept at about 120 fs. The spectral FWHM of the laser radiation is ∼12 nm centered around 800 nm. The laser beam is directed onto the sample by a system of mirrors; no focusing optics are used. The energy of the optical pulse is controlled by Schott neutral density glass filters. A thermopile power meter (Newport Inc., Irvine, CA) is used to measure the incident optical power. The maximum power available is 670 mW, which corresponds to

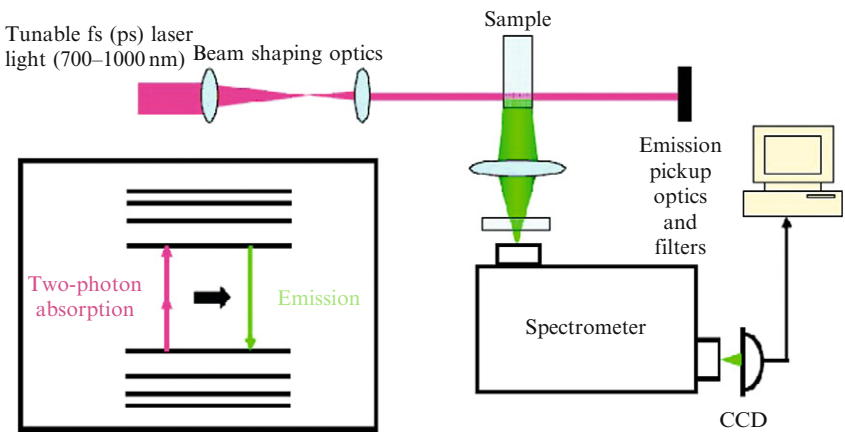

Figure 14.11 Schematic illustration of Laser irradiation/CF release detection setup.

670 μJ/pulse and an energy density of 16.1 mJ/cm^2 (or mean power density of 16.1 W/cm^2). The temperature of the HGN suspensions is measured using an Omegaette HH306 digital thermometer (Omega) with a K-type thermocouple probe (Omega Engineering Inc., Stamford, CT), which is immersed into the solution ~5 mm above the laser beam. The solution is stirred to ensure good mixing during irradiation.

Luminescence is excited in the sample via a two-photon absorption process. The emission is collected at a 90° angle by a system of lenses and focused on the entrance slit of a monochromator (Acton Research SpectraPro 300). The laser radiation is blocked by a Schott colored glass filter (BG38). The light dispersed by the monochromator is detected by a spectroscopic CCD camera (PI Acton PIXIS-400) and transferred into a personal computer for analysis. The evolution of the photoluminescence is recorded by collecting consecutive spectra over a 600 nm bandwidth with a constant interval. To quantify the fractional release of CF, fluorescence is measured using a PTI QuantaMaster spectrofluorimeter (Photon Technology International, Lawrenceville, NJ). Any release from the liposomes is detected by an increase in fluorescence intensity (from the background) as the external concentration of CF increased. The fractional release can be quantified as fractional release $= (I_{laser} - I_0)/(I_{max} - I_0)$, where I_{laser} is the fluorescence intensity of the solution after laser treatment, I_{max} is the maximum fluorescence intensity after lysing the liposomes with reduced Triton X-100 (a nonionic surfactant which has a hydrophilic polyethylene oxide group and a hydrophobic 4-(1,1,3,3-tetramethylbutyl)-phenyl group) (Boyer and Zasadzinski, 2007), and I_0 is the background fluorescence intensity before either treatment.

5.2. Continuous-wave laser irradiation

To illustrate the differences between pulsed and continuous-wave irradiation, the liposome/HGN samples are also irradiated with continuous NIR light, using a Spectraphysics 3900S Ti:Sapphire CW laser. The laser wavelength is tuned to 820 nm and the output power is controlled by changing the power of the pump laser source (Spectraphysics Beamlok-2060) to be 0.7 W. The Gaussian beam diameter of the CW laser is 1.0 mm.

6. Liposome Disruption and CF Release Due to Pulsed Laser Irradiation

Irradiation with femtosecond NIR light pulses with an energy density >2.2 W/cm^2 triggers a near instantaneous increase in the measured fluorescence in the solution of DPPC liposomes encapsulating HGNs and CF

Table 14.1 Comparison of triggered content release

Laser	Solution	Release (%)
Pulsed fs	CF	0 ± 2
	CF + Au NS	1 ± 2
	Liposomes containing CF, but no Au NS	-1 ± 2
	Au NS suspended freely outside of liposomes containing CF	28 ± 2
	Au NS and CF encapsulated inside liposomes	71 ± 1
	Au NS tethered to the outer surface of liposomes containing CF	93 ± 2
CW	Au NS and CF encapsulated inside liposomes	-1 ± 2

(Table 14.1), but has no effect on control solutions of unencapsulated CF, a mixture of HGNs and CF, or DPPC liposomes with CF, but no HGNs. In all samples, the CF concentrations are matched to give similar concentrations averaged over the sample volume. Continuous-wave (unpulsed) laser irradiation at 800 nm with a higher average power density of 89 W/cm^2 leads to no increase in the fluorescence intensity, and hence no CF release, even after 4 h of irradiation. When continuous-wave laser irradiation is used, the nanoshell is always close to being in thermal equilibrium with its surroundings, and there are insufficient temperature gradients to give rise to microbubble formation (Prasad *et al.*, 2005; Prevo *et al.*, 2008). From these observations, it is clear that minor changes in the solution and liposome temperature are not responsible for the rapid release of CF from the liposomes.

7. Mechanism of Triggered Liposome Release

To identify the mechanism of release, the laser power density is varied as in Fig. 14.9, while comparing the total fluorescence intensity after 9 min of irradiation with 120 fs long pulses at a 1 kHz repetition rate. Figure 14.12 shows a distinct power density threshold of NIR light necessary to trigger CF release from the liposomes: no fluorescence increase is detected for a power density lower than ~1.5 W/cm^2, while the total release is roughly constant at about 74% for power densities greater than 4.3 W/cm^2. The rate of fluorescence increase during NIR irradiation for liposomes encapsulating HGNs also increases with the laser power density (Fig. 14.13). The *in situ* fluorescence intensity is constant for an irradiation power density of 1.3 mJ/cm^2, which is below the threshold. Above the threshold, the curves could be fit with a single exponential, with a time constant increasing with decreased

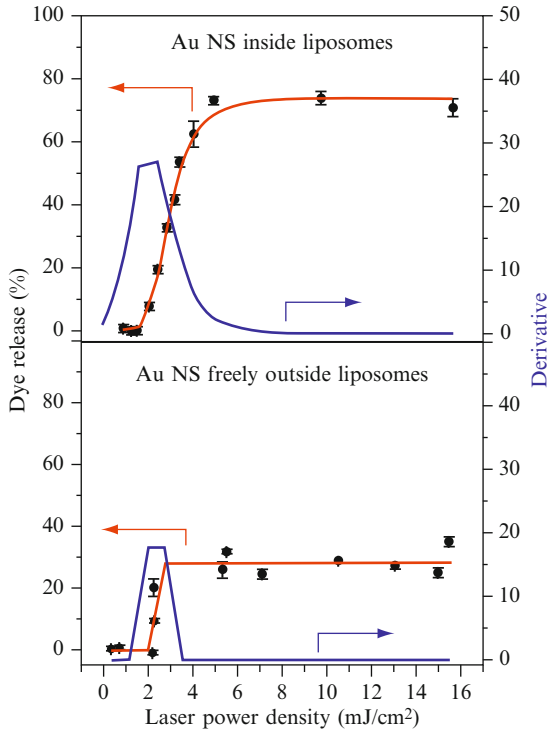

Figure 14.12 Effect of energy density on CR release from liposomes with HGNs encapsulated inside and suspended outside (black data points). The solid red curves are sigmoidal fits to the data; the blue curves are the derivative of the fit. The peak in the derivative gives the threshold energy for CF release, which is the same for both samples. The maximum release is quite different due to the different average distances between HGNs and the liposome bilayers.

laser power density (time constant $\tau = 5$, 52, and 112 at the power density of 14.9, 13.0, and 7.1 W/cm^2, respectively). At the higher power densities, release is complete within seconds.

The derivative of the release versus laser-energy density curves gives an estimate of the threshold energy density for contents release (Fig. 14.12). For both HGNs inside and free outside the liposomes, the threshold value is the same, $\sim$2.2 mJ/cm^2, which coincides with the threshold for the photoacoustic signal of cavitation in the solution (Fig. 14.9A). The power threshold suggests that the mechanism of triggered release is through perforation of lipid bilayers mediated by transient cavitation, that is, microbubble formation and collapse (Paliwal and Mitragotri, 2006; Pecha and Gompf, 2000; Tong *et al.*, 2007). Several recent studies have also suggested that the effects of plasmon-resonant nanoparticles on cell membrane rupture are

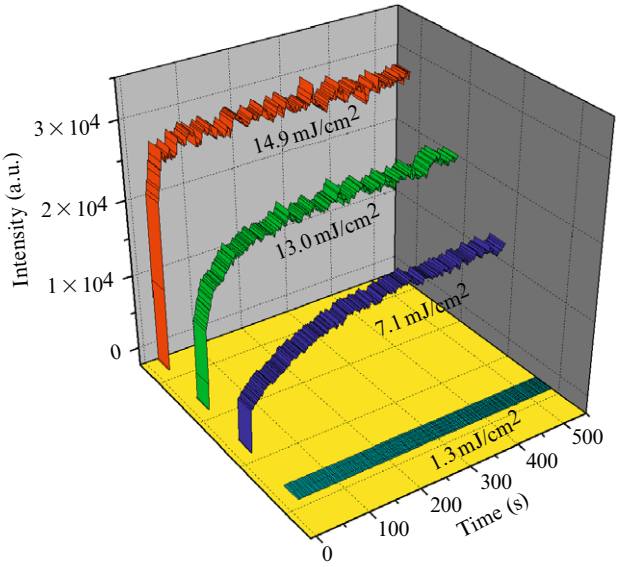

Figure 14.13 Kinetics of *in situ* fluorescence shows the rate of liposomal content-release induced by encapsulated HGNs at various laser-energy densities. Time zero is the beginning of laser irradiation. Below a threshold energy density (2.2 mJ/cm^2), there was no fluorescence increase. Above the threshold, there was a near instantaneous increase in the fluorescence intensity, followed by a more gradual increase. The increase of fluorescence increase can be fit by single exponential: $F = F_o + A\,e^{-x/\tau}$, with $\tau = 5$, 52, and 112 s at laser-energy densities of 14.9, 13.0, and 7.1 mJ/cm^2, respectively.

linked with cavitation dynamics and transient bubble formation (Lapotko *et al.*, 2006; Pitsillides *et al.*, 2003; Yao *et al.*, 2005.

While the permeability of DPPC liposomes increases near the gel to liquid crystalline transition temperature of 41 °C (Ponce *et al.*, 2006), this is not the source of the rapid increase in CF fluorescence observed here. The overall temperature increase of the solution due to the HGN absorption of NIR light is only a few degrees above ambient (Prevo *et al.*, 2008). Even at 41 °C, the permeability increase is only such that CF release would take minutes, not seconds as found here. The only way to get this rate of release is by the generation of large defects in the bilayer, as observed in liposomes after sonication (Zasadzinski, 1986). Only minor differences in liposome morphology are visible by cryo-EM after irradiation (Wu *et al.*, 2008); the bilayers are less spherical, and hence under less tension after irradiation, consistent with a decrease in the positive osmotic pressure difference following CF release. These minor changes in the liposome shapes or sizes after irradiation suggest that cavitation induces transient defects in the bilayer, enabling drug release, after which membrane integrity is restored.

8. Effect of Proximity of HGNs to Liposomes

Permeabilizing lipid membranes with microbubble cavitation should be induced by any HGNs in the solution, as long as there is an HGN within some maximum distance from a liposome bilayer. To test this hypothesis, DPPC liposomes encapsulating CF dye are mixed with increasing concentrations of HGNs, according to Scheme 14.2C. Upon pulsed laser irradiation, CF release is triggered. Figure 14.14 shows that the fractional CF release increases with HGN concentration up to an HGN concentration of 0.0315 m*M* (at higher HGN concentrations, the CF fluorescence is quenched by the HGNs (Dulkeith *et al.*, 2002), data not shown). Hence, increasing the HGN concentration allows more liposomes to be within a critical distance of an irradiated HGN, which causes more liposomes to be ruptured, leading to greater CF release and an increase in the fluorescence.

Minimizing and maintaining the distance between the HGN and the liposome bilayer lead us to tether HGNs to the outer surface of liposomes (Scheme 14.2B). Tethering the HGN directly to the outer surface of the liposomes increases the maximum release fraction to 96% (Table 14.1). The efficiency of phototriggered contents release is strongly affected by the proximity of HGN to the bilayer, consistent with the hypothesis that mechanical disruption by microbubbles is responsible for release (Tong *et al.*, 2007).

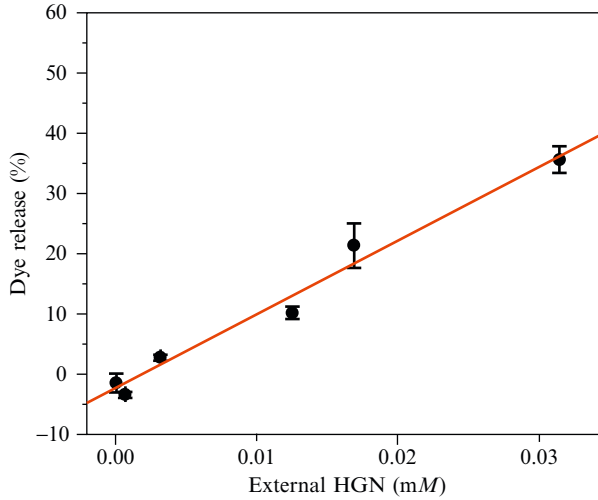

Figure 14.14 Effect of unencapsulated HGNs on CF release from DPPC liposomes after NIR irradiation at 16.1 mJ/cm^2. The solid line is a linear fit to the data.

9. Conclusions

Femtosecond pulses of NIR light absorbed by HGNs tethered to, encapsulated within, or in solution with liposomes trigger the near instantaneous release of liposome contents. The high temperatures reached by the HGN (Prasad *et al.*, 2005; Prevo *et al.*, 2008) induce production of unstable microbubbles, similar to the cavitation bubbles produced by ultrasound (Paliwal and Mitragotri, 2006). The mechanical and thermal effects of the microbubble collapse (Pecha and Gompf, 2000; Pitsillides *et al.*, 2003) causes disruption of the liposome carriers, similar to the disruption caused by sonication. Neither the liposomes nor the CF appears to be altered chemically during this process, and the overall temperature rise of the bulk solution is only a few degrees. NIR light can penetrate up to 10 cm into tissue, which should allow these liposome/HGN complexes to be addressed noninvasively within a reasonable fraction of the human body. Any liposome carrier could be modified by tethering or encapsulating HGN to produce a system for rapid release on demand via NIR irradiation. This should eventually allow for better control of drug delivery to selected disease sites while minimizing systemic toxicity.

ACKNOWLEDGMENTS

We thank Dr. Samir Mitragotri, Dr. Sumit Paliwal and Dr. Makoto Ogura for helpful discussions on cavitation and generously lending the hydrophone. This work was supported by the NIH Program of Excellence in Nanotechnology Grant HL080718: *Nanotherapy for Vulnerable Plaques*.

REFERENCES

Abraham, S. A., Waterhouse, D. N., Mayer, L. D., Cullis, P. R., Madden, T. D., and Bally, M. B. (2005). The liposomal formulation of doxorubicin. *Methods Enzymol.* **391,** 71–97.

Allen, T. M., and Cullis, P. R. (2004). Drug delivery systems: Entering the mainstream. *Science* **303,** 1818–1822.

Alvarez, M. M., Khoury, J. T., Schaaff, T. G., Shafigullin, M. N., Vezmar, I., and Whetten, R. L. (1997). Optical absorption spectra of nanocrystal gold molecules. *J. Phys. Chem. B* **101,** 3706–3712.

Bohren, C. F., and Huffman, D. R. (1983). Absorption and Scattering of Light by Small Particles. Wiley, New York, 530 pp.

Boyer, C., and Zasadzinski, J. A. (2007). Multiple lipid compartments slow vesicle contents release in lipases and serum. *ACS Nano* **1,** 176–182.

Chen, J., Wang, D., Xi, J., Au, L., Siekkinen, A., Warsen, A., Li, Z.-Y., Zhang, H., Xia, Y., and Li, X. (2007). Immuno gold nanocages with tailored optical properties for targeted photothermal destruction of cancer cells. *Nano Lett.* **7,** 1318–1322.

Chiruvolu, S., Warriner, H. E., Naranjo, E., Idziak, S., Radler, J. O., Plano, R. J., Zasadzinski, J. A., and Safinya, C. R. (1994a). A phase of liposomes with entangled tubular vesicles. *Science* **266,** 1222–1225.

Chiruvolu, S., Walker, S., Leckband, D., Israelachvili, J., and Zasadzinski, J. (1994b). Higher order self-assembly of vesicles by ligand-receptor interactions. *Science* **264,** 1753–1756.

Chiu, D. T., Wilson, C. F., Ryttsen, F., Stromberg, A., Farre, C., Karlsson, A., Nordholm, S., Gaggar, A., Modi, B. P., Moscho, A., Garza-Lopez, R. A., Orwar, O., *et al.* (1999). Chemical transformations in individual ultrasmall biomimetic containers. *Science* **283,** 1892–1895.

Davidsen, J., Jorgensen, K., Andresen, T. L., and Mouritsen, O. G. (2003). Secreted phospholipase A(2) as a new enzymatic trigger mechanism for localised liposomal drug release and absorption in diseased tissue. *Biochim. Biophy. Acta* **1609,** 95–101.

Discher, B. M., Won, Y. Y., Ege, D. S., Lee, J.-M., Bates, F. S., and Hammer, D. (1999). Polymersomes: Tough vesicles made from diblock copolymers. *Science* **284,** 1143–1146.

Dulkeith, E., Morteani, A. C., Niedereichholz, T., Klar, T. A., Feldmann, J., Levi, S. A., van Veggel, F. C. J. M., Reinhoudt, D. N., Moller, M., and Gittins, D. I. (2002). Fluorescence quenching of dye molecules near gold nanoparticles: Radiative and nonradiative effects. *Phys. Rev. Lett.* **89,** 203002/203001–203002/203004.

Frederick, P. M., and Hubert, D. H. (2005). Cryoelectron microscopy of liposomes. *Methods Enzymol.* **391,** 431–448.

Grua, P., Morreeuw, J. P., Bercegol, H., Jonusauskas, G., and Vallee, F. (2003). Electron kinetics and emission for metal nanoparticles exposed to intense laser pulses. *Phys. Rev. B Condens. Matter Mater.* **68,** 035424/03542.1–035424/0354.12.

Hao, E., Li, S. Y., Bailey, R. C., Zou, S. L., Schatz, G. C., and Hupp, J. T. (2004). Optical properties of metal nanoshells. *J. Phys. Chem. B* **108,** 1224–1229.

Harris, N., Ford, M. J., and Cortie, M. B. (2006). Optimization of plasmonic heating by gold nanospheres and nanoshells. *J. Phys. Chem. B* **110,** 10701–10707.

Hirsch, L. R., Stafford, R. J., Bankson, J. A., Sershen, S. R., Rivera, B., Price, R. E., Hazle, J. D., Halas, N. J., and West, J. L. (2003). Nanoshell-mediated near-infrared thermal therapy of tumors under magnetic resonance guidance. *Proc. Natl. Acad. Sci. USA* **100,** 13549–13554.

Huang, S.-L. (2008). Liposomes in ultrasonic drug and gene delivery. *Adv. Drug Deliv. Rev.* **60,** 1167–1176.

Huang, S.-L., and MacDonald, R. C. (2004). Acoustically active liposomes for drug encapsulation and ultrasound-triggered release. *Biochim. Biophy. Acta* **1665,** 134–141.

Huang, X., El-Sayed, I. H., Qian, W., and El-Sayed, M. A. (2006). Cancer cell imaging and photothermal therapy in the near-infrared region by using gold nanorods. *J. Am. Chem. Soc.* **128,** 2115–2120.

Johnson, P. B., and Christy, R. W. (1972). Optical constants of the noble metals. *Phys. Rev. B* **6,** 4370–4379.

Jung, H. T., Lee, S. Y., Coldren, B., Zasadzinski, J. A., and Kaler, E. W. (2002). Gaussian curvature and the equilibrium between cylinders, discs and spheres. *Proc. Natl. Acad. Sci. USA* **99,** 15318–15322.

Kisak, E. T., Coldren, B., and Zasadzinski, J. A. (2002). Nanocompartments enclosing vesicles, colloids, and macromolecules via interdigitated lipid bilayers. *Langmuir* **18,** 284–288.

Kisak, E. T., Coldren, B., Evans, C. A., Boyer, C., and Zasadzinski, J. A. (2004). The vesosome—A multicompartment drug delivery vehicle. *Curr. Med. Chem.* **11,** 199–219.

Kotaidis, V., Dahmen, C., von Plessen, G., Springer, F., and Plech, A. (2006). Excitation of nanoscale vapor bubbles at the surface of gold nanoparticles in water. *J. Chem. Phys.* **124,** 184702/184701–184702/184707.

Kreibig, U. (1977). Anomalous frequency and temperature dependence of the optical absorption of small gold particles. *J. Phys. (Paris) Colloq.* **2,** 97–103.

Kreibig, U., and Genzel, L. (1985). Optical absorption of small metallic particles. *Surf. Sci.* **156,** 678–700.

Kreibig, U., and Vollmer, M. (1995). *In* "Optical Properties of Metal Clusters," Springer Series in Materials Science, 532 pp.

Lapotko, D. O., Lukianova, O. E., and Oraevsky, A. A. (2006). Selective laser nano-thermolysis of human leukemia cells with microbubbles generated around clusters of gold nanoparticles. *Lasers Surg. Med.* **38,** 631–642.

Liang, H. P., Wan, L. J., Bai, C. L., and Jiang, L. (2005). Gold hollow nanospheres: Tunable surface plasmon resonance controlled by interior-cavity sizes. *J. Phys. Chem. B* **109,** 7795–7800.

Lin, C. P., and Kelly, M. W. (1998). Cavitation and acoustic emission around laser-heated microparticles. *Appl. Phys. Lett.* **72,** 2800–2802.

Link, S., Burda, C., Nikoobakht, B., and El-Sayed, M. A. (1999a). How long does it take to melt a gold nanorod? A femtosecond pump-probe absorption spectroscopic study. *Chem. Phys. Lett.* **315,** 12–18.

Link, S., Wang, Z. L., and El-Sayed, M. A. (1999b). Alloy formation of gold-silver nanoparticles and the dependence of the plasmon absorption on their composition. *J. Phys. Chem. B* **103,** 3529–3533.

Mueller, A., Bondurant, B., and O'Brien, D. F. (2000). Visible-light-stimulated destabilization of PEG-liposomes. *Macromolecules* **33,** 4799–4804.

Niidome, T., Yamagata, M., Okamoto, Y., Akiyama, Y., Takahashi, H., Kawano, T., Katayama, Y., and Niidome, Y. (2006). PEG-modified gold nanorods with a stealth character for *in vivo* applications. *J. Control. Release* **114,** 343–347.

Noble, C. O., Kirpotin, D. B., Hayes, M. E., Mamot, C., Hong, K., Park, J. W., Benz, C. C., Marks, J. D., and Drummond, D. C. (2004). Development of ligand-targeted liposomes for cancer therapy. *Expert Opin. Ther. Targets* **8,** 335–353.

Norman, R. S., Stone, J. W., Gole, A., Murphy, C. J., and Sabo-Attwood, T. L. (2008). Targeted photothermal lysis of the pathogenic bacteria, pseudomonas aeruginosa, with gold nanorods. *Nano Lett.* **8,** 302–306.

Oldenburg, S. J., Averitt, R. D., Westcott, S. L., and Halas, N. J. (1998). Nanoengineering of optical resonances. *Chem. Phys. Lett.* **288,** 243–247.

Paliwal, S., and Mitragotri, S. (2006). Ultrasound-induced cavitation: Applications in drug and gene delivery. *Expert Opin. Drug Deliv.* **3,** 713–726.

Pecha, R., and Gompf, B. (2000). Microimplosions: Cavitation collapse and shock wave emission on a nanosecond time scale. *Phys. Rev. Lett.* **84,** 1328–1330.

Peer, D., Karp, J. M., Hong, S., Farokhzad, O. C., Margalit, R., and Langer, R. (2007). Nanocarriers as an emerging platform for cancer therapy. *Nat. Nanotechnol.* **2,** 751–760.

Petrova, H., Perez Juste, J., Pastoriza-Santos, I., Hartland, G. V., Liz-Marzan, L. M., and Mulvaney, P. (2006). On the temperature stability of gold nanorods: Comparison between thermal and ultrafast laser-induced heating. *Phys. Chem. Chem. Phys.* **8,** 814–821.

Pitsillides, C. M., Joe, E. K., Wei, X., Anderson, R. R., and Lin, C. P. (2003). Selective cell targeting with light-absorbing microparticles and nanoparticles. *Biophys. J.* **84,** 4023–4032.

Ponce, A. M., Vujaskovic, Z., Yuan, F., Needham, D., and Dewhirst, M. W. (2006). Hyperthermia mediated liposomal drug delivery. *Int. J. Hyperthermia* **22,** 205–213.

Popinet, S., and Zaleski, S. (2002). Bubble collapse near a solid boundary: A numerical study of the influence of viscosity. *J. Fluid Mech.* **464,** 137–163.

Prasad, V., Mikhailovsky, A., and Zasadzinski, J. A. (2005). Inside-out disruption of silica/gold core-shell nanoparticles by pulsed laser irradiation. *Langmuir* **21,** 7528–7532.

Prevo, B. G., Esakoff, S. A., Mikhailovsky, A., and Zasadzinski, J. A. (2008). Scalable routes to gold nanoshells with tunable sizes and properties: Monitoring their response to NIR pulsed laser irradiation. *Small* **4,** 1183–1195.

Roper, D. K., Ahn, W., and Hoepfner, M. (2007). Microscale heat transfer transduced by surface plasmon resonant gold nanoparticles. *J. Phys. Chem. C* **111,** 3636–3641.

Schwartzberg, A. M., Oshiro, T. Y., Zhang, J. Z., Huser, T., and Talley, C. E. (2006). Improving nanoprobes using surface-enhanced Raman scattering from 30-nm hollow gold particles. *Anal. Chem.* **78,** 4732–4736.

Sengupta, S., Eavarone, D., Capila, I., Zhao, G., Watson, N., Kiziltepe, T., and Sasisekharan, R. (2005). Temporal targeting of tumour cells and neovasculature with a nanoscale delivery system. *Nature* **436,** 568–572.

Shi, W., Sahoo, Y., Swihart, M. T., and Prasad, P. N. (2005). Gold nanoshells on polystyrene cores for control of surface plasmon resonance. *Langmuir* **21,** 1610–1617.

Shum, P., Kim, J.-M., and Thompson, D. H. (2001). Phototriggering of liposomal drug delivery systems. *Adv. Drug Deliv. Rev.* **53,** 273–284.

Simões, S., Fonseca, C., Pedroso de Lima, M., and Düzgüneş, N. (2006). pH responsive liposomes. State of the art from biophysics to therapy. *In* "Smart Nanoparticles in Nanomedicine," (R. Arshady and K. Kono, eds.), Vol. 8, pp. 217–250. Kentus Books, London.

Sou, K., Endo, T., Takeoka, S., and Tsuchida, E. (2000). Poly(ethylene glycol)-modification of the phospholipid vesicles by using the spontaneous incorporation of PEG into the vesicles. *Bioconjug. Chem.* **11,** 372–379.

Sun, Y. G., and Xia, Y. N. (2004). Mechanistic study on the replacement reaction between silver nanostructures and chloroauric acid in aqueous medium. *J. Am. Chem. Soc.* **126,** 3892–3901.

Sun, Y. G., Mayers, B. T., and Xia, Y. N. (2002). Template-engaged replacement reaction: A one-step approach to the large-scale synthesis of nanostructures with hollow interiors. *Nano Lett.* **2,** 481–485.

Sun, Y., Mayers, B., and Xia, Y. (2003). Metal nanostructures with hollow interiors. *Adv. Mater.* **15,** 641–646.

Tong, L., Zhao, Y., Huff, T. B., Hansen, M. N., Wei, A., and Cheng, J.-X. (2007). Gold nanorods mediate tumor cell death by compromising membrane integrity. *Adv. Mater.* **19,** 3136–3141.

Turkevich, J. (1985). A history of colloidal gold. *Gold Bull.* **18,** 86–91.

Turkevich, J., Stevenson, P. C., and Hillier, J. (1951). A study of the nucleation and growth processes in the synthesis of colloidal gold. *Dis. Faraday Soc.* **11,** 55–65.

Turkevich, J., Garton, G., and Stevenson, P. C. (1954). The color of colloidal gold. *J. Colloid Sci.* **9,** S26–S35.

Weissleder, R. (2001). A clearer vision for *in vivo* imaging. *Nat. Biotechnol.* **19,** 316–317.

Wiley, B., Herricks, T., Sun, Y. G., and Xia, Y. N. (2004). Polyol synthesis of silver nanoparticles: Use of chloride and oxygen to promote the formation of single crystal, truncated cubes and tetrahedrons. *Nano Lett.* **4,** 1733–1739.

Wiley, B., Sun, Y. G., Chen, J. Y., Cang, H., Li, Z. Y., Li, X. D., and Xia, Y. N. (2005). Shape controlled synthesis of silver and gold nanostructures. *MRS Bull.* **30,** 356–361.

Wu, G., Mikhailovsky, A., Khant, H. A., Fu, C., Chiu, W., and Zasadzinski, J. A. (2008). Remotely triggered liposome release by near-infrared light absorption via hollow gold nanoshells. *J. Am. Chem. Soc.* **130,** 8175–8177.

Yao, C. P., Rahmanzadeh, R., Endl, E., Zhang, Z., Gerdes, J., and Huttmann, G. (2005). Elevation of plasma membrane permeability by laser irradiation of selectively bound nanoparticles. *J. Biomed. Opt.* **10,** 064012/064011–064012/064018.

Zalipsky, S., Brandeis, E., Newman, M. S., and Woodle, M. C. (1994). Long circulating, cationic liposomes containing amino-peg-phosphatidylethanolamine. *FEBS Lett.* **353,** 71–74.

Zasadzinski, J. A. (1986). Transmission electron microscopy observations of sonication-induced changes in liposome structure. *Biophys. J.* **49,** 1119–1130.